

## **CONTROLLING GRAIN EVOLUTION OF IN625 PARTS PRODUCED BY LPBF-AM**

E. Palmer, J. Rosser, M. Ritchie, C. Bromley, S. G. R. Brown and N. P. Lavery

Faculty of Science and Engineering, Swansea University, Swansea, SA1 8EN.

### **Abstract**

Laser Powder Bed Fusion (LPBF) Additive Manufacturing (AM) is rapidly being adopted globally due to its capability of producing complex net-shape parts in a range of alloys with mechanical properties as good as, or better than conventional processes. The alluring possibility is in controlling microstructural features during processing such as grain size, solidification morphology and texture, giving mechanical properties tailored for intended applications. LPBF-AM microstructures are dominated by sizeable columnar growth, which along with even small levels porosity contribute to lower fatigue and creep strength in comparison to wrought. This would limit high temperature applications where IN625 is used in aeroengine exhaust sections. In contrast, the less dominating equiaxed grains lead to a reduction in crack propagation and improve fatigue performance at the surface. In this work a combination of physical experiments and modelling is used to study the controllability of grain growth and orientation of IN625 made by LPBF-AM.

### **Introduction**

Over the years Laser Powder Bed Fusion (LPBF) Additive Manufacture (AM) technologies have received increasing interest across all industries due to the possibility of producing highly functional, near-net shape parts with a minimised amount of post-processing steps. In particular, the increased degrees of freedom presented by this process has allowed industries, such as the aerospace industry, to produce parts that were previously not possible leading to safer systems with higher efficiencies.

Due to the combination of high-strength, fatigue resistance, and anti-corrosion properties [1], IN625 is an excellent candidate for such an industry. IN625 is capable of performing at extreme temperatures for extended periods of time, with resistance to oxidation and carburisation. This is due to the stiffening effect of niobium and molybdenum on the nickel-chromium matrix, these elements also contribute to the alloy's resistance and performance in highly corrosive environments.

Despite the benefits presented by LPBF-AM, there are key challenges to face. The unique thermal cycle and rapid cooling rates often create complex microstructures and phases that attribute to anisotropic mechanical properties [2], changes in porosity and surface finishes. These issues present a new challenge, with the control of grain structures and crystallographic textures in metals being an area of key significance along with the manufacture of tailored parts for specific applications.

Previous attempts to control grain structures in LPBF-AM have returned varying levels of success with the focus on changes in scanning strategy, which are often achieved at the expense of build times. The focus of this study is manipulation of laser parameters within the built part via changes in volumetric energy density (V.E.D) and its effect on grain evolution mechanisms. Changes in laser power (W) and speed (m/s) alter the size and shape of the melt pool behind the path of the laser. In turn, this effects the temperature gradient (G) along with the liquid/solid interface velocity (R). These parameters were devised by models of heat

transfer and provide good approximation of the columnar to equiaxed transition (CET) of an alloy produced via LPBF-AM [3].

## Materials and Methods

### *Inconel 625 Powder*

Within this work, the IN625 powder used was supplied by Sandvik Osprey with powder size distributions of Dx(10), Dx(50) and Dx(90) values of 25.4, 34.8 and 47.0  $\mu\text{m}$  (measured by particle size analysis), respectively and a composition show in table 1. samples were then built using Renishaw's AM400 which utilises a 400W ytterbium fibre laser with a 70  $\mu\text{m}$  spot size. In addition, the reduced build volume (RBV) auxiliary was also used for rapid testing of various alloys (although, IN625 was the sole focus in this study).

Ni	Cr	Mo	Fe	Nb	Al	C	Si	Co	Mn	Ti	O	N	P	S
62	21.7	8.9	3.8	3.74	0.007	0.02	0.02	<0.01	0.01	<0.01	0.009	0.003	<0.003	<0.001

*Table 1. Chemical composition of IN625 (wt.%)*

### *Selective Laser Melting*

There are five controllable parameters that lead to differing volumetric energy densities. Point distance, PD ( $\mu\text{m}$ ) refers to the distance the laser moves laterally between spots. Hatch spacing, HS ( $\mu\text{m}$ ) is the parallel distance between two laser lines. Exposure time, ET ( $\mu\text{s}$ ) refers to the time heat is applied to a singular point. Power, P (W) is the wattage output up to a maximum of 400W in the case of this study. The scanning speed, V (m/s) is calculated by dividing point distance by exposure time. The oxygen level in the build chamber was reduced to under 0.1% by introducing Argon gas creating an inert atmosphere.

The volumetric energy density, V.E.D ( $\text{J}/\text{mm}^3$ ) can be defined as the volume of energy input to the material per millimetre cubed and is calculated through equation 1 and describes the relationship between these parameters. layer thickness, LT ( $\mu\text{m}$ ) remained at a constant 60  $\mu\text{m}$  for all builds.

$$VED = \frac{P}{V.HS.LT} = \frac{P.ET}{PD.HS.LT} \quad (1)$$

For this study, nine density cubes were built using differing parameters as seen in table 2. A tenth configuration was also built using the suggested parameters set out by Renishaw. The substrate under each cube was the optimised configuration named the crucible.

### *Density Optimisation*

Each cube was analysed by a method based on Archimedes principle; density measurements were taken for all 10 samples using the sigma 700/701 force tensiometer. Water was used as the suspension fluid but was combined with an emulsifier so that breaks in surface tension would not result in inaccurate values for density. Temperature of the air and water were recorded, with initial mass values and change in mass after each test, from this, density in  $\text{g}/\text{cm}^3$  could be calculated along with porosity from the theoretical density. Density could then be

calculated as a percentage with the normalised density being calculated from the densest sample, assuming it to be 100% dense.

For further verification, the cubes were then sectioned and prepared for optical porosity analysis using the Zeiss Observer to view the XY and XZ planes in full view. Scanning electron microscope (SEM) imaging was undertaken with a JEOL JSM-6010PLUS.

ImageJ was used to analyse the captured images. This was done by formatting the image and adjusting the threshold so that porosity was the area of interest. Readouts can then be given for average size and area of porosity, working backwards from this, density measurements can be obtained for each sample. The results from these are given in table 3.

Table 2. Inconel 625 Build Parameters

Sample Label	PD ( $\mu\text{m}$ )	HS ( $\mu\text{m}$ )	ET ( $\mu\text{s}$ )	PW (W)	V (m/s)	V.E.D ( $\text{J}/\text{mm}^3$ )
A1	70.00	70.00	45.00	300.00	1.56	45.92
A2	70.00	80.00	60.00	350.00	1.17	62.50
A3	70.00	90.00	75.00	400.00	0.93	79.37
A4	80.00	70.00	60.00	400.00	1.33	71.43
A5	80.00	80.00	75.00	300.00	1.07	58.59
A6	80.00	90.00	45.00	350.00	1.78	36.46
A7	90.00	70.00	75.00	350.00	1.20	69.44
A8	90.00	80.00	45.00	400.00	2.00	41.67
A9	90.00	90.00	60.00	300.00	1.50	37.04
Ren (AR)	70.00	70.00	40.00	400.00	1.75	54.42

### Simulation Model

Melt pool simulations were produced via the heat equation for welding simulations as presented in: Eagar, T. and Tsai, N. (1983) "Temperature Fields Produced by Traveling Distributed Heat Sources" [4]. Melt pool geometry was calculated using both measured and sourced thermophysical properties (see Table 3), namely, absorption (A), density ( $\rho$ ), specific heat capacity ( $C_p$ ), the solidus temperature ( $T_s$ ), the liquidus temperature ( $T_L$ ), the critical temperature ( $T_c$ ) and the thermal conductivity (k). The solution uses a gaussian heat distribution in dimensionless form to indicate final melt pool shape to accurately predict weld pool shapes for specified alloy systems. This was computed using a MATLAB script and compared against experimental data.

A	$\rho$ ( $\text{kg}/\text{m}^3$ )	$C_p$ ( $\text{J}/\text{kg}\cdot\text{K}$ )	$T_s$ (K)	$T_L$ (K)	$T_c$ (K)	k ( $\text{W}/\text{m}\cdot\text{K}$ )
0.46	8440	451.67	1581.05	1653.65	9460	9.36

Table 3. Thermophysical properties of Inconel 625 (solid state)

From these simulations values for the temperature gradient (G) and solidification velocity (R) could be found. The temperature gradient is the gradient of temperature across which growth morphology occurs in crystalline metals. Given by:

$$G = \Delta T \quad (2)$$

The solidification velocity is the ratio of the solidification cooling rate within the metal to the temperature gradient given by:

$$\frac{\delta T}{\delta t} = \frac{T_S - T_L}{t_S - t_L} \quad (3)$$

where  $T_L$  and  $T_S$  are the liquidus and solidus temperatures reached at times  $t_L$  and  $t_S$  respectively.

Giving solidification velocity (R) as:

$$R = \frac{1}{G} \frac{\delta T}{\delta t} \quad (4)$$

### Layered Builds

Further to the original 10 builds, a layered sample was produced that consisted of a cube built with a high energy density with regions of lower energy density embedded in eight layers of varying thicknesses. Each layer is an  $8 \times 8 \times X$  mm where  $X$  is varied from 0.1-1 mm. The high and low energy density layers contained the same parameter sets as A3 and A6 respectively, this is shown in figure 1.

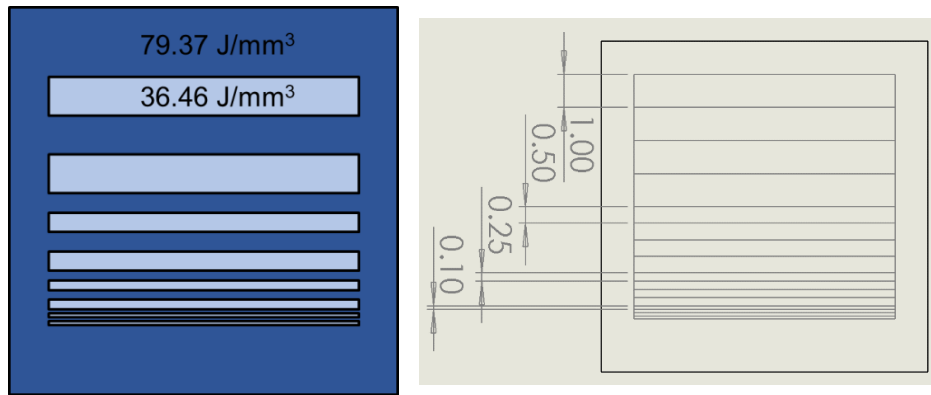


Figure 1. layered build showing energy density layers (left) dimension of layers (right, dimensions in mm).

### Metallographic Preparation

Each sample was removed from the build plate using a bandsaw to cut through the supports, a BUEHLER IsoMet 4000 precision saw was used to face the samples, with the density cubes being cut in the XY and XZ directions and the layered build being cut in the XZ direction as this was parallel to the grains being observed. Each sample was mounted via hot compress in conductive bakerlite with a BUEHLER SimpliMet XPS1 mounting system. The samples were then polished with a BUEHLER AutoMet 250 and EcoMet 250 pro grinder-polisher. The procedure was as follows: 400 to 1200 grit Si grinding pad until plane, then 9, 6 and 1 $\mu$ m water-based diamond polish with polishing pad each for ten minutes. The layered sample was then etched in a mixed acids reagent, 15ml:10ml:10ml - Hydrochloric Acid, Acetic Acid and Nitric Acid. The samples were immersed for 5 to 10 seconds at room temperature before washing off with ethanol and drying. The density cube samples were not etched as analysis of the porosity was the focus in contrast to the microstructure.

## Results and discussion

### *Density Optimisation*

The experimental values are shown in table 3. Figure 2 shows experimental density of both Archimedes and optical compared with V.E.D.

Figure 2 shows a near uniform density within the builds, with A3 providing the greatest density and the Renishaw optimised settings producing near 100% density when normalised with the other builds. The lower density samples of A6 and A8 typically correlate with a lower volumetric energy density indicating more porosity within the build. There appears to be an anomalous result with the A9 build, due to having one of the lowest V.E.D it was expected to have a greater amount of porosity but appears nearly 100% dense when a density of 96-98% was expected.

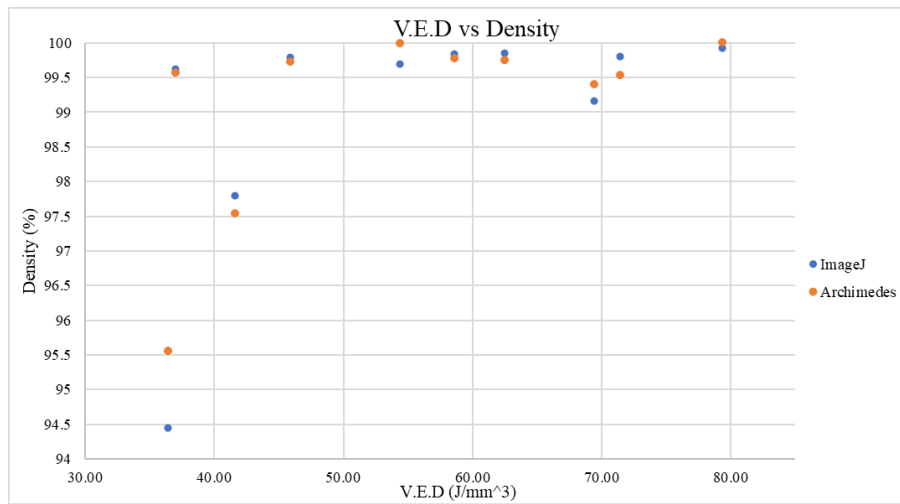


Figure 2. Graph of volumetric energy density ( $J/mm^3$ ) vs density (%)

Table 4. Values of V.E.D and density

Sample Label	V.E.D ( $J/mm^3$ )	Density (%)	Density Normalised (%)	Density from ImageJ (%)
<b>A1</b>	45.92	103.43	99.730	99.784
<b>A2</b>	62.50	103.41	99.752	99.849
<b>A3</b>	79.37	103.49	100.000	99.913
<b>A4</b>	71.43	103.19	99.531	99.802
<b>A5</b>	58.59	103.20	99.772	99.839
<b>A6</b>	36.46	99.04	95.557	94.442
<b>A7</b>	69.44	102.95	99.400	99.153
<b>A8</b>	41.67	101.14	97.535	97.796
<b>A9</b>	37.04	103.20	99.571	99.610
<b>AR</b>	54.42	103.14	99.986	99.689

Figures below show the surface of density cube samples A6, A3 and AR. As expected, there is a direct and visible correlation between V.E.D and porosity, with higher V.E.D leading to less porosity. No microstructure can be seen in these images without etchants. A6 possesses the greatest amount of porosity of the three builds, with large volumes of inclusions created by

escaping gasses during the build process. At low V.E.D, there is often incomplete laser coverage causing high levels of porosity. High density samples such as A3 still contain small amounts of porosity but often with large areas of no visible porosity. Scratches are often seen on the surface; these are caused by the dislodging of un-melted powders within inclusions which are dragged across the surface when polishing. These scratches could be removed with thresholding in ImageJ as to not skew the data.

For sample A3, the density calculated from ImageJ is largely similar to the tested density but is slightly lower due to the visibility of porosities, whereas the tested density had been normalised to 100% due to being the densest sample. For the Renishaw build, the tested density and density from ImageJ were largely concurrent, with ImageJ slightly overestimating. There is a large disparity with the A6 samples of around 4%. The captured images were in the XY plane parallel to the build plate, due to these porosities being defects from build parameters, the captured images may exaggerate the volume of porosity as there is no gauge of depth in the images.



Figure 3. A6 XY (left) A3 XY (centre) AR XY (right)

### Electron Microscopy and EBSD

Figures 4(a) and (b) show the A6 sample at varying magnifications in both the XY and XY directions. These samples had been etched prior to imaging. Within these images some porosity can be seen and it's important to see how microstructural changes occur when interacting with porosity and inclusions. Figure 4(a) shows the melt pool profiles and 'fish mouthing' caused by the outline of the melt pools, both figures 4(a) and (b) show the cellular dendritic growth of the microstructure within each layer, this growth is common within LPBF-AM alloys [5] and is often referred to as constrained growth. Both coarse and elongated cells can be seen in figure 4(b), often adjacent to each other. Figure 4(b) shows these different microstructures broken up via coloured lines. It is postulated that this type of growth is caused by competition between Molybdenum and Niobium as they separate on cooling causing a hexagonal sub structure [6]. Future work may include an EDS map to verify the composition of these grains. The elongated cells show epitaxial growth over the fish mouthing where the coarser cells do not. This is due to the re-melting of several layers during frequent passes of the laser. This has allowed for the grain growth process to restart in each subsequent layer [7]. There is a theory that the coarse cells don't experience overlapping with various layers, so are not remelted by subsequent laser passes and don't experience the same energy input in the form of heat, causing a stall of the grain growth process leading to the formation of a coarser microstructure, often referred to as unconstrained growth [8]. It can also be seen how porosity stops the formation of elongated cells whereas the coarser, more hexagonal cells tend to conform around them. This agrees with the previous argument of layer remelting as the escape of gas causing porosity would be several layers deep causing no remelting of the layers and subsequently no grain growth. The irregular inclusion seen in figure 4(b) may have been caused

by a defect in the build such as a line defect due to the parameters used, the lack of laser passes would explain the absence of elongated cells but the presence of some hexagonal cells.

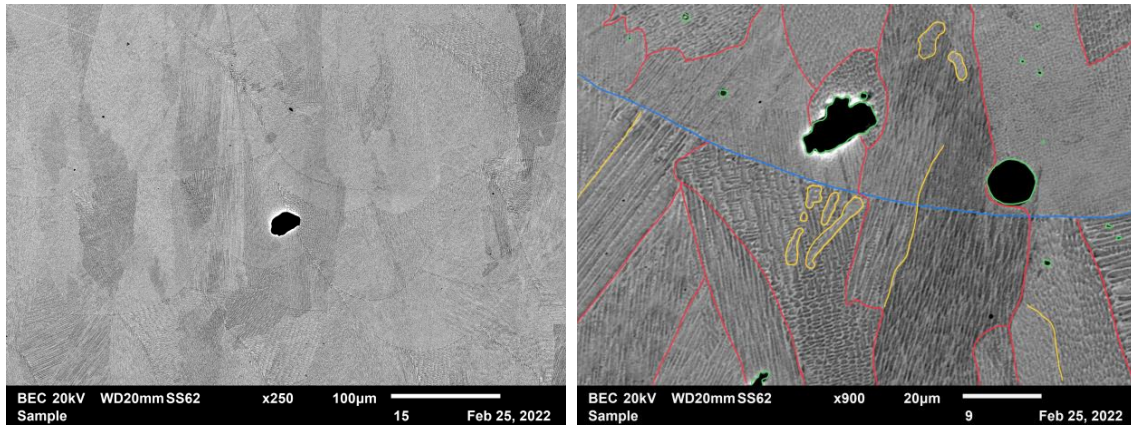


Figure 4. SEM Image of A6 XY (a) SEM Image of A6 XY, green lines show porosity, red lines show distinction between coarse and elongated grains, blue lines show the melt pool profile, yellow lines show secondary phases within grains (b).

### *EBSD Layered Sample*

Figures 5 and 6 contain the images of the etched layered sample containing layers of energy densities corresponding to A3 and A6. The image is characterised by alternating light and dark bands corresponding to differing volumetric energy densities. The lower V.E.D layers are characterised by light bands containing large amounts of porosity. The higher V.E.D is slightly darker with a more uniform surface texture. The greatest presence of observable microstructures occurs at the boundaries between different V.E.D and in the bulk of the thicker layers of greater energy density. Coarser cells are more common within the lower energy density layers but are also seen in the higher energy density layers. As seen in figure 5, the layers are encased within a boundary of the higher energy density, this extends to every face of the sample and can be thought of as a cube within a cube. There also appears to be more microstructural features in the surrounding perimeter giving rise to the elongated cells and the darker blue colour. This is due to the greater number of laser passes in those specific areas, imparting more heat energy causing elongated cells and grain growth.

As the presented images are in the XZ plane, these cells are nucleating upwards, perpendicular to the build plate. In “Fundamentals of solidification” by W. Kurz, Kurz postulates that these elongated cells grow along the direction of the thermal gradient and in a preferred crystallographic orientation, whereas the smaller, coarser like grains could grow between the thermal gradient and their preferred orientation [9]. This concurs with what can be seen in figure 6, elongated cells are most present on the melt pool boundaries and tend to grow perpendicularly into the melt [10] and often transition to more equiaxed coarser grains within the melt pool boundaries, this would be along the thermal gradient of the melt pool. As previously stated, the elongated cells can grow epitaxially across melt pool lines but are stopped almost instantly when reaching a region of differing volumetric energy density, whereas there are a few examples of coarse equiaxed grains crossing over melt pool lines, but they tend to be uncommon.

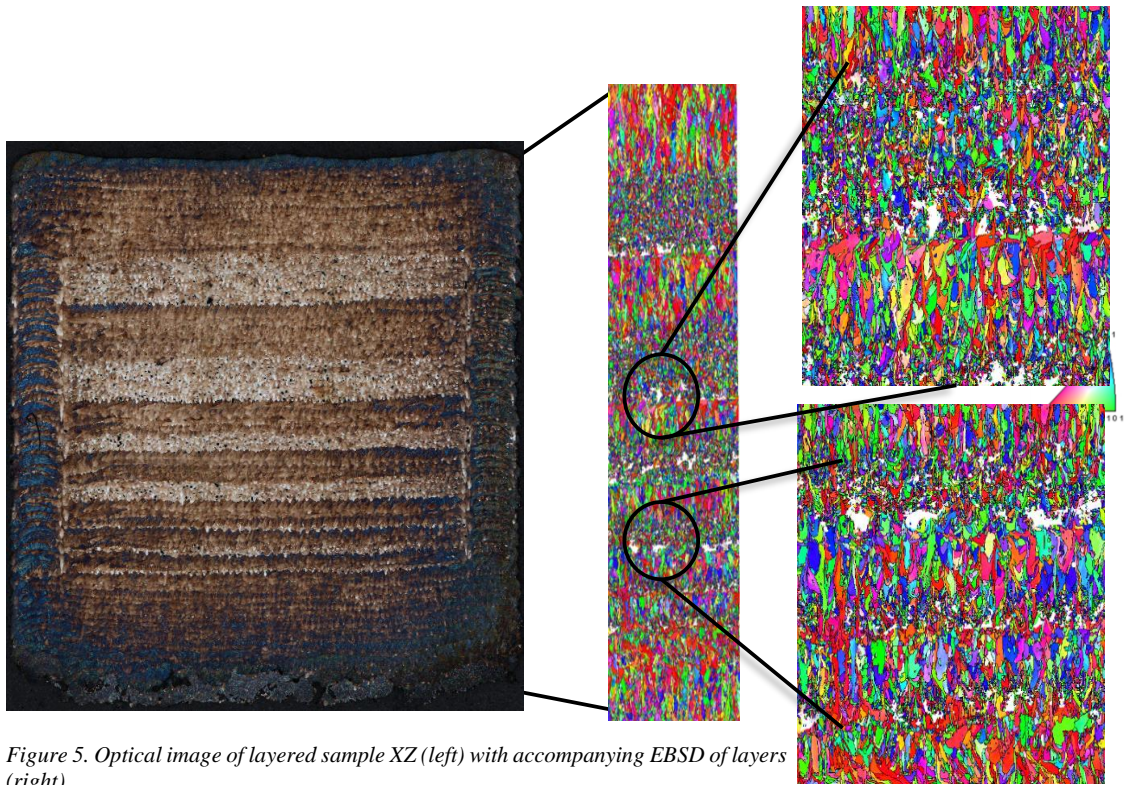


Figure 5. Optical image of layered sample XZ (left) with accompanying EBSD of layers (right).

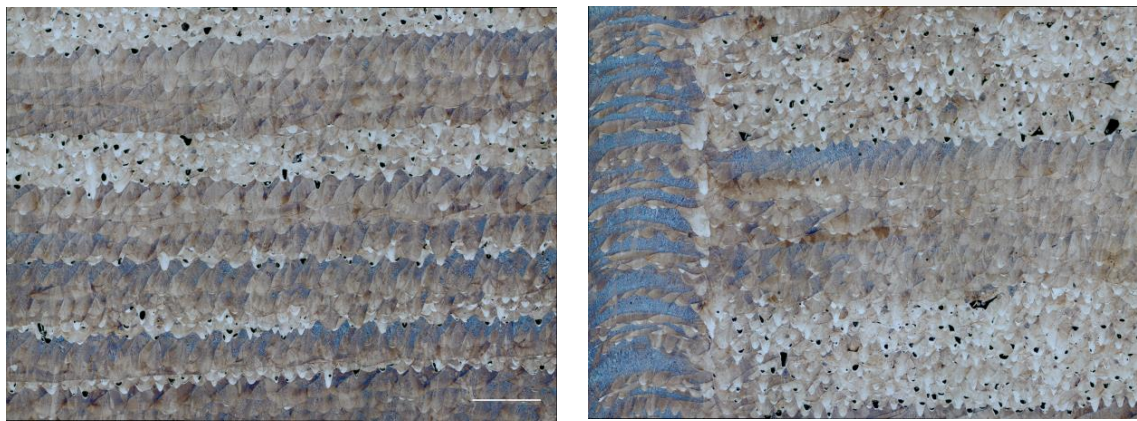


Figure 6. Optical image of layered sample XZ top centre (left) top left (right).

This layered sample was also analysed via EBSD, shown in figure 5, and largely agreed with the optical analysis seen. Columnar grain growth was more apparent in the regions of high energy density and when undisturbed, climbed through the part in the build direction whereas this growth was inhibited in the lower energy density region where equiaxed grains were formed. In addition, porosity was also seen to affect grain growth in a similar way. Columnar growth is paused below the pores and equiaxed growth begins above it as seen in this SEM image.

*Simulation Work*

Melt pool dimensions were taken from experimental values and those given computationally within MATLAB from Eagar and Tsai’s solution, across a range of scan speeds and powers (table 4), this data is shown in figure 7. There were a broader range of depth values for those taken experimentally compared to the values taken from MATLAB, there may be two reasons for this. The plots produced by MATLAB include the entire heat effected zone of the melt, so only values above the solidus temperature should be taken to calculate the melt pool size. It is important to note that the Rosenthal solution used in these simulations does not account for the latent heat of transformation within the set metal parameters along with the nonlinear effects of temperature-dependent properties [11]. This produces temperature estimations vastly greater than the evaporation temperature of IN625 which were not achieved during the practical builds hence everything above the liquidus temperature was largely ignored. Other issues arise when comparing against captured images, there are large amounts of overlapping of melt pools within the build which is to be expected but means accurate calculation of melt pool depth was more difficult with greater variance. Two value sets are given for the depths calculated via Eagar and Tsai’s solution which relate to the laser absorptivity values used. As this value was unknown, a sensitivity study was conducted which revealed a value of 0.8 gave more accurate depth measurements. A data set using a value of 0.2 has also been included to show the variability between possible parameter values.

*Table 5. Computational combinations of power (W) and speed (m/s)*

<b>Power/Speed Combination (30 Runs Total)</b>	
<b>Power (W)</b>	<b>Speed (m/s)</b>
300	0.2
	0.4
	0.6
	0.8
350	1.0
	1.2
	1.4
	1.6
400	1.8
	2.0

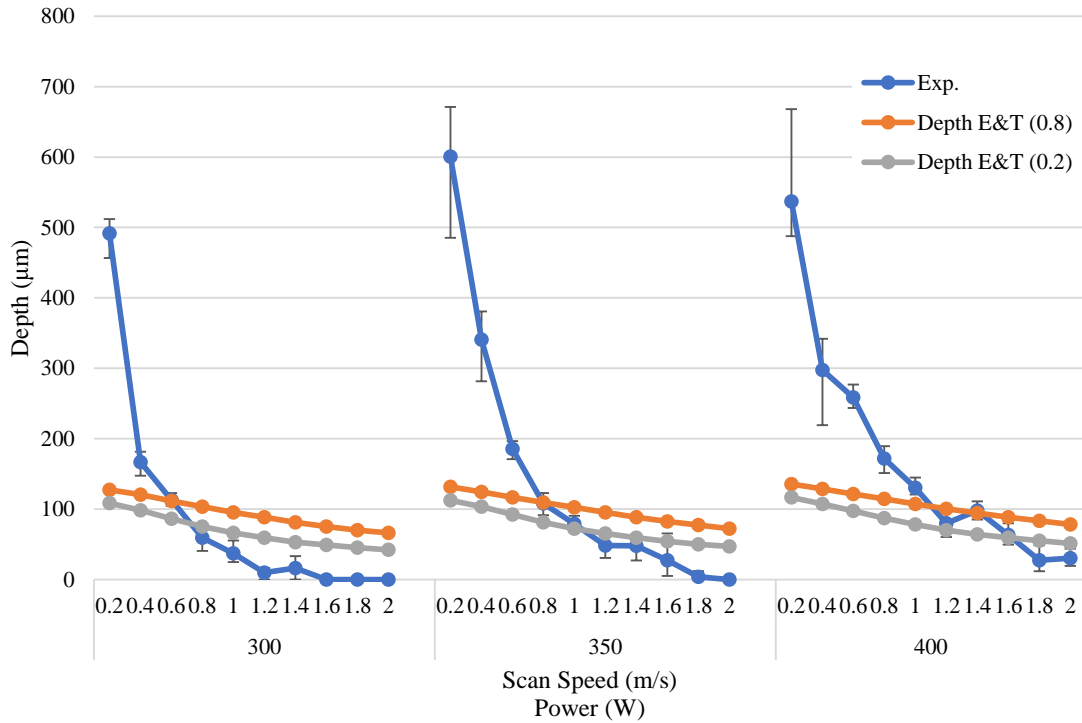


Figure 7. Depth plot as a function of scan speed and power for experimental data (blue) and computational data (orange/grey).

#### Columnar to Equiaxed Transition (CET) Plot

Columnar to equiaxed transition (CET) curves use values of  $G$  (thermal gradient) and  $R$  (solidification velocity) to determine whether the morphology of a grain will be columnar, equiaxed or a mixture between the two. The determination of these states is based on where values fall around two mathematically derived curves called Hunt criterion lines. These curves are based on statistical probability of grain growth from an initial dendrite. If a value falls below the equiaxed dendrite line at which the volume fraction of equiaxed dendrites is greater than 49% this area corresponds to a fully equiaxed grain morphology. If a value exceeds the columnar dendrite line, at which the volume fraction of equiaxed dendrites is less than 0.66%, the grain morphology is seen as fully columnar. Between these two lines the grain morphology is estimated to be a mixture of columnar and equiaxed.

Using equations 2-4 in conjunction with the data from MATLAB, a CET graph was able to be plotted, seen in figure 8. It is shown that as V.E.D is increased the likelihood of columnar growth becomes more apparent, conversely, application of a lower V.E.D would result in a mixture of columnar and equiaxed. This is largely agreeable with both the optical and EBSD analysis of the layered sample, with energy densities corresponding to A3 ( $79.37 \text{ J/mm}^3$ ) exhibiting strong columnar growth and energy densities corresponding to A6 ( $36.46 \text{ J/mm}^3$ ) exhibiting more equiaxed growth. For all power and speed combinations modelled, the thermal gradient saw very little variation compared to the solidification velocity. The thermal gradient was expected to decrease with increasing depth and increasing solidification velocity. It is also shown how solidification rate is highly dependent on process parameters.

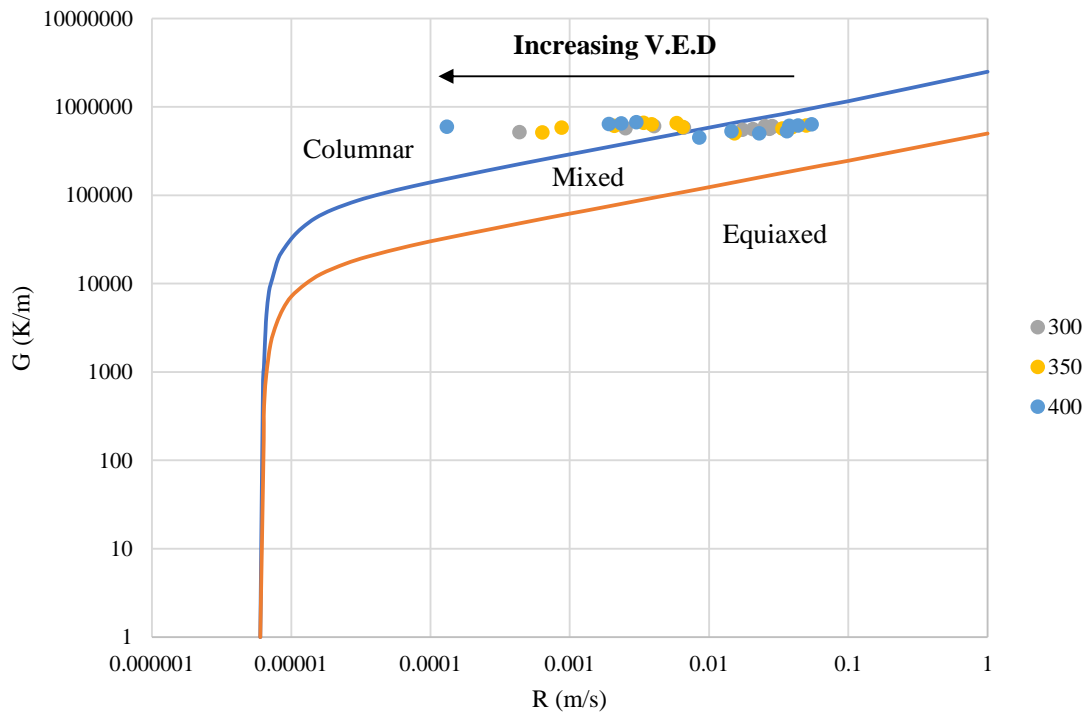


Figure 8. CET Plot of thermal gradient and solidification velocity against a range of process parameters.

## Conclusion

IN625 was used in conjunction with LPBF-AM to investigate grain morphology growth mechanisms during applications of varied energy density. The process parameters were first optimised through means of density measurements, first based on Archimedes principle, then optically through ImageJ. This provided two main parameter sets with one high volumetric energy density corresponding to A3 ( $79.37 \text{ J/mm}^3$ ) and one low volumetric energy density corresponding to A6 ( $36.46 \text{ J/mm}^3$ ), Renishaw's optimised parameter set AR was also used in comparison with the optical density measurements.

Firstly, scanning electron microscopy was used as a microstructural analysis tool in effort to understand how porosity effects grain growth, this revealed two main sub-cellular cell

structures, coarser and elongated grains. The presence of these grains was due to the heat energy imparted by the laser which differed based on the volumetric energy density of each build. These structures exhibited different growth mechanisms across melt pool lines and around porosity.

Secondly, a layered build consisting of alternating layers of volumetric energy in varying thicknesses was produced. This enabled different grain growth mechanisms to be seen when crossing boundaries of differing volumetric energy density, it was shown optically that columnar grains grew preferentially in higher V.E.D, but their growth was stopped immediately when reaching a boundary of two differing layers. More equiaxed grains grew in both high and low energy densities and exhibited some ability to grow across the boundaries of two layers but this tended to be infrequent. EBSD was carried out on the layered sample and agreed with what was seen, columnar grain growth was more apparent in the regions of high energy density and when undisturbed, climbed through the part in the build direction whereas this growth was inhibited in the lower energy density region where equiaxed grains were formed.

Finally, simulation-based work was carried out within MATLAB to measure melt pool size and shape, but some disparity was observed when comparing with values measured experimentally. The melt pool profiles produced via MATLAB included the entire heat effected zone, not just the liquid melt. Values taken experimentally were often crowded with other melt pool lines making distinction and measurement more difficult. Using MATLAB, values for the thermal gradient ( $G$ ) and the solidification velocity ( $R$ ) were calculated and plotted on a columnar to equiaxed transition (CET) curve. It was shown that as V.E.D is increased, the likelihood of columnar growth becomes more apparent, conversely, application of a lower V.E.D would result in a mixture of columnar and equiaxed grains, this was in agreeance with what was seen both optically and through EBSD on the layered sample.

### References

- [1] V. Shankar, K. Bhanu Sankara Rao, S.L. Mannan, Microstructure and mechanical properties of Inconel 625 superalloy, *Journal of Nuclear Materials*, Volume 288, Issues 2–3, Pages 222-232. 2001.
- [2] V.A. Popovich, E.V. Borisov, A.A. Popovich, V.Sh. Sufiiarov, D.V. Masaylo, L. Alzina, Functionally graded Inconel 718 processed by additive manufacturing: Crystallographic texture, anisotropy of microstructure and mechanical properties, *Materials & Design*, Volume 114, Pages 441-449. 2017.
- [3] W. Kurz, C. Bezençon & M. Gäumann, Columnar to equiaxed transition in solidification processing, *Science and Technology of Advanced Materials*, 2:1, 185-191. 2001.
- [4] Eagar, T. and Tsai, N, Temperature Fields Produced by Traveling Distributed Heat Sources. *Welding Journal*, 62, 346-355. 1983.
- [5] S. Sanchez, P. Smith, Z. Xu, G. Gaspard, C. J. Hyde, W. W. Wits, I. A. Ashcroft, H. Chen, A. T. Clare, Powder Bed Fusion of nickel-based superalloys: A review, *International Journal of Machine Tools and Manufacture*, Volume 165. 2021.
- [6] Y. Wang, C. Zhang, Construction of Cellular Substructure in Laser Powder Bed Fusion, *Metals*, vol. 9, no. 11, p. 1231. Nov. 2019

- [7] M. Calandri, S. Yin ,B. Aldwell, F. Calignano, R. Lupoi, D. Ugues. Texture and Microstructural Features at Different Length Scales in Inconel 718 Produced by Selective Laser Melting. Materials (Basel). 2019.
- [8] K. Gola, B. Dubiel, I. Kalembe-Rec, Microstructural Changes in Inconel 625 Alloy Fabricated by Laser-Based Powder Bed Fusion Process and Subjected to High-Temperature Annealing. Journal of Materials Engineering and Performance. 29. 2020.
- [9] D. Fisher, K. Wurcz, Fundamentals of solidification, fourth edition, Trans Tech Publications. 1986.
- [10] A. A. Ferreira, A. R. Reis, R. L. Amaral, J. M. Cruz, P. C. Romio, J. O. Seabra, M. F. Vieira, Mechanical and microstructural characterisation of bulk Inconel 625 produced by direct laser deposition, Materials Science and Engineering: A, Volume 838. 2022.
- [11] S. Bontha, The effect of Process Variables On Microstructure in Laser-Deposited Materials M.S., Wright State University. 2002.